Supporting Information

Saatchi et al. 10.1073/pnas.1019576108

SI Materials and Methods

Overview. Our approach consists of four steps: (*i*) processing of ground and Geoscience Laser Altimeter System (GLAS) Lidar observations to sample forest structure and biomass over tropical regions, (*ii*) developing relations between Lidar-derived Lorey's height and AGB and between AGB and BGB, (*iii*) mapping forest biomass carbon (AGB + BGB) at 1-km spatial resolution using satellite imagery to stratify tropical forest types and structure and modeling the spatial distribution using the maximum entropy (MaxEnt) approach, and (*iv*) assessing the uncertainty in modeling the spatial distribution by validating the results and propagating the errors through the methodology to estimate the total carbon stock and its uncertainty at project and national scales.

(i) Processing of in situ and GLAS data. In situ forest inventory data. We assembled 4,079 plots that spanned a variety of forest types on each continent, including old growth moist and wet tropical forest, woodland savanna, dry forest, peat swamp forest, and forests recovering from past disturbance or clearing. These ground data used to train the biomass prediction model were derived from various sources including published literature and national forest inventories collected by the authors and their colleagues (Table S1). Although these measurements do not follow a uniform systematic inventory protocol (they vary in plot size, sampling scheme, allometric equations, and number of structural components), they have produced the largest known dataset on forest aboveground biomass density throughout the tropics. The plots included in this study met the following criteria: (*i*) All biomass measurements were made after 1995 and before 2005 so that the resulting biomass map would be representative of forest biomass circa the year 2000. (*ii*) Plots had a minimum size of 0.1 ha and the biomass densities represented all trees >10 cm in diameter. For pixels that included multiple plots, we used the average biomass value of all plots weighted by the plot size. We used a minimum area of 1 ha from one one plot or a combination of smaller plots to sample the biomass density of 1-km pixels and eliminated all pixels with less plot area from the analysis. A total of 1,877 1-km pixels from inventory plots were used in the analysis (Fig. S1). The sampling errors were included in the uncertainty analysis (described below) of the forest biomass map.

ICESat GLAS Lidar data. To compensate for the lack of systematic spatial sampling of aboveground biomass from ground measurements, we included a method for estimating biomass from satellite Lidar measurement of forest vertical structure. Data from the GLAS, onboard the Ice, Cloud, and land Elevation Satellite (ICESat), acquired in 2003 and 2004 over tropical forests were used in this study. GLAS is a waveform sampling Lidar sensor; it emits short duration (5 ns) laser pulses toward the land surface and records the echo of those pulses as they reflect off the ground surface (1). When the surface is vegetated, the return echoes, or waveforms, are a function of the vertical distribution of vegetation and ground surfaces within the area illuminated by the laser (the footprint). For forests on level ground, stand height can be calculated as the difference between the elevation of the first returned energy minus the mean elevation of the ground return (waveform extent) (2). The vertical extent of each waveform increases as a function of terrain slope and footprint size (the area on the ground that is illuminated by the laser), as modified by the spatial pattern of ground surfaces visible to the laser. Over sloped terrain, information on the vertical extent of the waveform is insufficient to make estimates of tree height. Therefore, algorithms capable of retrieving information about terrain slope, stand uniformity, and the vertical distribution of visible ground surfaces from the waveform itself were used for terrain slope corrections (3, 4).

To estimate forest height from Lidar waveform indexes, a model developed from several study areas in broadleaf stands in temperate and tropical forests was used (5). The model was calibrated with three study areas with ground estimates of height in the Amazon basin, located in the municipalities of Santarem, Para State; Manaus, Amazonas State; and Canarana, Mato Grosso State, all in Brazil. These sites represented areas with a range of dry season duration (months with <100 mm of rain). Dry season duration was selected as an environmental variable that was likely to summarize structural trends across the Amazon (6).

The index of height derived from field measurements and used in the processing of the global GLAS dataset is Lorey's height, the basal area weighted height of all trees >10 cm in diameter,

$$H_{\text{lorey}} = \frac{\sum_{i=1}^{N} \text{BA}_i h_i}{\sum_{i=1}^{N} \text{BA}_i}, \qquad \textbf{[S1]}$$

where BA_i and h_i are the basal and canopy heights of individual trees in a plot. Basal area weighting of tree heights increases the importance of the largest trees in a stand and represents the height of stands with tallest trees. Indexes of total waveform extent and the height of the 10th and 90th percentiles of waveform height were used with least-squares regression to estimate Lorey's height (5). An equation to estimate Lorey's height for broadleaf stands explained 83% of variance with an RMSE of 3.3 m or 17.3% of relative error (5).

We processed ~3 million Lidar Lorey's heights derived from GLAS shots distributed over tropical forests (523,985 in Africa, 1,583,557 in Latin America, and 974,392 in Asia). All GLAS heights derived for terrains with slopes >20% were deleted from the dataset because of potential errors in Lorey's height estimates (4). The terrain slope was calculated from shuttle radar topography mission (SRTM) data at 90 m spatial resolution coincident with Lidar footprints.

Estimation of AGB from Lidar data. Lorey's heights derived from GLAS data were converted to AGB using 493 calibration plots. The calibration plots were located under the GLAS footprints or within the same forest stand and represented the forest structure sampled by GLAS Lidar. Each plot had an area of at least 0.25 ha that was equal to or larger than the effective footprint area of GLAS (<0.5 ha) Lidar samples (5) and included tree height, basal area, and genera-specific wood density for all trees >10 cm in diameter at breast height (dbh). The plots covered a wide range of forest types. In Latin America, 298 plots were distributed in terra firme forests of the Central Amazon in Manaus (Amazonia), Santarem (Para), and Camarana (Mato Grosso); seasonal transitional forests of Rondonia (Ji Parana); and forests of the western Amazonia in Peru including terra firme, bamboo, and seasonally flooded forests (Manu, Tampopata). In Africa, 75 plots covered the forest–savanna transitions of Mbam-Djerrem (Cameroon); old growth forests in Budongo (Uganda), Cavalla and Grebo (Liberia), Ekobakoba, Oveng, and Dousalla (Gabon); and old growth and successional forests in Lope National Park (Gabon). In Asia, 120 plots covered old growth, secondary, and logged forests in Sabah (Malaysia) (Table S2).

We estimated the aboveground biomass for all individual trees in calibration plots using pan-tropical generalized allometric equations developed by Chave et al. (7). For woodland savanna

plots, the dry forest equation, AGB = $0.112(\rho D^2 h)^{0.916}$, and for all other plots, the moist forest equation, AGB = $0.0509(\rho D^2 h)$, were used to estimate AGB (ρ is the wood density, D is dbh, and h is the tree height). In these equations, tree heights were accounted for by direct measurements with clinometers and laser range finders for almost all trees (DBH > 10 cm), and diameter-based estimation was used for a small fraction where no direct height measurements were available (8).

The tree height measurements from the calibration plots were used to develop a relationship between Lorey's height and the estimated AGB at the plot level. The new allometric equations were derived separately for each continent and for the combined dataset (Fig. 1). After evaluating the equations by cross-validating with data from each continent, we concluded that continent-based equations provided the best model to convert Lorey's height to forest biomass. The equations were then used to convert GLAS Lidar height data to AGB for all available GLAS footprints over tropical forests and woodlands.

Differences in equations can be attributed to several factors: (*i*) The number of plots used in each continent and the sampling strategy to capture the forest types and structure are different. In Asia, the plots were equally distributed in old growth, secondary forests, logged forests, and plantations. In South America plots were mainly from old growth forests, with a small portion in secondary and swamp forests. Plots in Africa were almost equally divided between dense old growth forests and woodland savanna. (*ii*) Wood density is used in estimating the biomass of trees for each plot. Differences in wood density of large trees in each continent can bias the equation converting Lorey's height to biomass. Potentially, by including wood density, differences in continental equations could be reduced.

Next, we used the average of at least five AGB values of Lidar footprints in 1-km pixels to create 160,918 pixels (80,579 pixels in Africa, 37,931 pixels in America, and 42,408 pixels in Asia). The 1-km pixel data were subsequently divided into training data (93,188 pixels) and test data (67,730 pixels) for AGB modeling, validation, and uncertainty analysis. The geographical distribution of 1-km pixels with average Lorey's height along with available ground data is shown in Fig. S1.

BGB estimation from AGB. We encountered virtually no consistent measurements of belowground biomass in our data compilation efforts. This result was not surprising, as measurement methods for collecting belowground biomass data are laborious, time-consuming, and technically challenging to perform correctly. Instead, belowground biomass is usually estimated from aboveground biomass using regression equations developed from field data collected across multiple biomes (9). A synthesis of data from available literature, along with elimination of data collected using unclear or incorrect methods, provided a universal equation for estimating forest belowground biomass. We used this equation to estimate belowground biomass from aboveground biomass estimated for each 1-km forested pixel in our analysis,

$$\text{BGB} = 0.489\text{AGB}^{0.89}, \qquad \textbf{[S2]}$$

where BGB is the belowground and AGB is the aboveground biomass in units of megagrams per hectare of dry weight. To develop an uncertainty in the above relationship, we acquired the data from Mokany et al. (9) and examined the variations in the ratio of below:aboveground biomass or root:shoot biomass ratios with respect to vegetation types used in the study. By excluding sites in forest plantations and grasslands and tundra, the RMSE in predicting the belowground biomass was 9.46 Mg ha^{-1} with relative error of ~23.2% (Fig. S2). Once belowground biomass was calculated from aboveground biomass, we calculated the total as the sum of above- and belowground estimates and converted the results to live tree carbon content by using a conversion factor of 0.5. In our analysis, we have ignored all

other components of the Intergovernmental Panel on Climate Change carbon pools such as dead wood and litter due to lack of data and models to estimate from aboveground biomass.

(ii) Spatial modeling of AGB. There are multiple ways of extrapolating the samples of forest biomass data to a gridded map. These include parametric approaches such as the use of regression models with spatial environmental data and nonparametric approaches such as interpolation, cokriging, classification or coloring by numbers, decision rule techniques as in random forest, MaxEnt, and several machine learning approaches (10–12). Parametric models are not suitable for extrapolating the biomass data because there is no reasonable relationship that exists between current satellite observations (passive optical and microwave) and tropical forest biomass. In addition, parametric models often violate conditions of independence and multivariate normality when complex ecological systems and environmental variables derived from different remote sensing measurements are involved. Nonparametric models are found to be more suitable in geospatial and geostatistic analysis because they are not affected by these violations, can integrate variables with different statistical distributions, and provide more stable and relevant information. Furthermore, forest structure and biomass often exhibit complex, nonlinear variations, autocorrelation, and variable interaction across temporal and spatial scales. In these cases, nonparametric approaches often greatly outperform the parametric methods (11).

Among nonparametric models, we selected MaxEnt after comparing its performance against two other methods (random forest and maximum-likelihood classification), using a set of training and test datasets. In all cases, MaxEnt outperformed the other methods in modeling the spatial distribution of biomass and in providing significantly better accuracy compared with an independent dataset.

MaxEnt is a general-purpose algorithm that generates predictions or inferences from an incomplete set of information. The MaxEnt approach is based on a probabilistic framework. It relies on the assumption that an incomplete empirical probability distribution, which is based on individual occurrences of a variable's point locality in geographical space (here, biomass sample points from ground and GLAS Lidar), can be approximated with a probability distribution that has maximum entropy (the MaxEnt distribution) subject to certain environmental constraints and that this distribution approximates potential geographic distribution (12, 13). For our purposes, we assume the unknown probability distribution P is defined over a finite set X (interpreted as the set of pixels within the study area), with the probability value of $P(x)$ for each point x. These probabilities sum to 1 over the space defined by X. The MaxEnt algorithm uses a Bayesian approach to approximate P with a probability distribution $\widehat{\mathbf{P}}$ by maximizing the entropy of $\widehat{\mathbf{P}}$ as

$$\text{Entropy} = \sum_{x \in X} \widehat{\mathbf{P}}(x)\ln\left[\widehat{\mathbf{P}}(x)\right], \qquad \textbf{[S3]}$$

where ln is the natural logarithm. Entropy is a nonnegative number with the maximum value equal to the natural log of the number of pixels in X and is a measure of constraints or choices of a probability distribution. The distribution $\widehat{\mathbf{P}}$ with highest entropy (i.e., the least additional information is introduced through model assumptions), while still subject to the constraints of incomplete information, is considered the best distribution for inference. By using features that are continuous real-valued functions of X, such as remote sensing variables, and a set of sample points (training data) of X provided by the field data and GLAS Lidar points, the MaxEnt algorithm employs likelihood estimation procedures to find a probability distribution for all of the points in X that have similar statistics to the sample points. MaxEnt assumes a priori a uniform distribution and performs

a number of iterations in which the weights (of different features) are adjusted to maximize the average probability of the point localities (also known as the average sample likelihood), expressed as the training gain (13). These weights are then used to compute the MaxEnt distribution over the entire geographic space. In the context of the present study, MaxEnt can be applied to geographic locations of forest plots and remote sensing data to produce distributions expressing the suitability (probability) of each pixel as a function of the environmental variables of that pixel. A high value of the probability function for a particular pixel indicates that the pixel is predicted to be suitable for having similar characteristics to the training pixels (12). MaxEnt has a number of properties that make it useful for modeling forest biomass over landscapes (12, 13). These properties include a deterministic framework (and hence stability), high performance with relatively few sample points, good computing efficiency (which enables the use of large-scale, high-resolution data layers), continuous output (i.e., from least to most suitable conditions), and the ability to model complex responses to environmental or remote sensing variables. The MaxEnt model has a built-in jackknife option, which allows estimation of the significance of individual data layers in the computation of the final distributions.

The spatial modeling with MaxEnt included three steps: (*i*) compiling the spatially gridded remote sensing data, (*ii*) implementation of MaxEnt and the production of the AGB map, and (*iii*) estimation of prediction uncertainty.

Compiling remote sensing data. We compiled a set of remote sensing data and products from different earth observing sensors to derive metrics sensitive to vegetation cover, density, seasonality, moisture, roughness, and surface topography. The dataset included both optical and microwave satellite sensors. All optical data used in this study are from the moderate resolution imaging spectroradiometer (MODIS) aboard the Terra satellite. We included normalized difference vegetation index (NDVI) and leaf area index (LAI) products. MODIS products were downloaded from the Earth Resources Observation and Science Data Center (ftp://e4ftl01.cr.usgs.gov/MOTA/) from the latest iteration of MODIS product development (collection 5, MOD13A35) and processed for cloud cover and pixel quality.

We used LAI to develop landscape-scale data layers related to vegetation canopy structure and seasonality as an important feature to stratify the forest and the NDVI data as a measure of vegetation greenness that generally correlates well with ground measurements of gross photosynthesis (14).

Both NDVI and LAI data were processed to develop cloud-free monthly images for the years 2000–2001. For pixels that did not have any values because of MODIS quality flags and cloud contamination, we used the best data from the same months over the next few years (2001–2003) to fill gaps. The monthly data were then used to generate three LAI metrics, annual maximum, mean, and range (difference of maximum and minimum); and five NDVI metrics, maximum NDVI, mean NDVI, green NDVI (average of greenest or highest NDVI quarter), brown NDVI (average of brownest or lowest NDVI quarter), and NDVI green–brown (difference between highest and lowest NDVI quarters) (15).

As part of the microwave remote sensing measurements, we included global quick scatterometer (QSCAT) data available in 3-d composites at 2.25-km resolution (16). The 3-d time series data in the year 2000 were used to create average monthly composites at a 1-km resolution and were then further processed to produce four metrics that included annual mean and SD of radar backscatter at both HH and VV polarizations (H, horizontal send/receive; V, vertical send/receive). QSCAT radar measurements are at KU band (12 GHz) and are sensitive to surface or canopy roughness, moisture, and other seasonal attributes, such as phenological changes, although the relationship between QSCAT and specific forest variables is yet to be explored. For areas with low vegetation biomass, such as woodlands and savanna, measurements at different polarizations correlate positively with the aboveground biomass. For areas with dense forest, backscatter measurements are sensitive to canopy roughness and moisture and contribute to measuring differences in forest types and canopy structure. In this study, we used the long-term mean and SD of QSCAT HH backscatter data and excluded the VV backscatter data because of its high correlation with the HH backscatter over tropical forests (16). In addition two seasonality metrics of average HH backscatter from dry and wet quarters were added to the list of input variables.

We added the SRTM digital elevation data, aggregated from ~90-m resolution to 1 km, in the pool of spatial data layers. In addition to the mean elevation, the SD of surface elevation was calculated during pixel aggregation from 90-m to 1-km resolution and was also included as a metric to represent landforms or geological features with different ruggedness or topographical variability (17, 18). We used the SRTM layers along with the rest of the remote sensing data to model the distribution of forest ecological variables. We also included the MODIS-derived vegetation continuous field (VCF) product as a measure of the percentage of tree canopy cover within each 1-km pixel resolution (19). The VCF product was not used in spatial modeling of AGB, but used later to estimate total carbon stock for forests above 10%, 25%, and 30% tree cover.

MaxEnt implementation. We ran the MaxEnt model using the locations of inventory plots and GLAS Lidar points over forests of all three tropical regions, using 14 remote sensing image layers (5 NDVI, 3 LAI, 4 QSCAT, and 2 SRTM metrics). The total number of biomass pixels from inventory plots was 1,877 and that from GLAS Lidar points was 160,918. Although, the number of inventory plots was much smaller than that of GLAS Lidar points, it provided biomass samples with less uncertainty and in regions where there were no GLAS Lidar tracks. From the combined dataset, we randomly selected 93,188 points to train the model and used the rest as an independent dataset to examine the accuracy of the resulting map. Aboveground biomass density from the training data were divided into 11 biomass classes in 25 Mg ha^{-1} intervals for biomass ranging from 0 to 100 Mg ha^{-1} and 50 Mg ha^{-1} intervals for biomass >100 Mg ha^{-1}. Biomass classes were used partially to capture the errors associated with the GLAS-derived biomass values and partially because MaxEnt does not run with continuous data (13). However, biomass ranges for each class can be easily modified as long as there are enough samples (>100 locations) within each class bin. We ran MaxEnt for different biomass ranges to examine the impact on the final AGB map and we found the selected biomass ranges suitable for creating the optimum map. For each interval (biomass class), we performed a MaxEnt model run and generated 11 continuous probability distribution maps ranging from 0 to 100, with 0 as the least suitable pixel for the biomass class and 100 as the most suitable. The continuous probability maps were then combined and converted into a single biomass map by choosing the biomass value associated with the maximum probability weighted mean for each pixel, using the relationship

$$\hat{B} = \frac{\sum_{i=1}^{N} p_i^n B_i}{\sum_{i=1}^{N} P_i^n}, \qquad \textbf{[S4]}$$

where P_i is the MaxEnt probability estimated for each biomass range class B_i (median value of the range), and $\hat{B}$ is the predicted value of AGB for each pixel. The power of the probability n is chosen to weight the predicted value toward the maximum probability that is close to the true value when other class probabilities are small. After several iterations and cross-validation with the test data, we found that for $n = 3$ the distribution of AGB and the cross-validation converged to its optimum value.

This process also preserved the skewness in distributions for each pixel, which by definition is the third standard moment ($n = 3$) of the random variable (biomass) defined by the probability distributions at each pixel. Values $>n = 3$ did not change the estimated biomass at the pixel scale (<0.001% of pixels changed values in each continent). The estimator in Eq. S4 performed superior to other options such as the use of maximum probability class or the average ($n = 1$). In both cases, errors associated with the estimated biomass were large. In the case of average value ($n = 1$), areas of low and high biomass values were forced to the mean biomass of the distribution over the region. On the other hand, the choice of maximum probability class ignored the probability of other classes for the same pixel. We could not use any other simple and efficient estimator such as the maximum likelihood because at any pixel the estimated probabilities of the biomass did not have a normal distribution. For example, for a pixel with a biomass class range of 200–250 Mg ha^{-1}, MaxEnt predicts high probability for the correct biomass range, suggesting a skewed and nonnormal distribution of probabilities. In general, AGB of a cluster of pixels at the landscape scale may have normal distribution. However, the predicting probability of biomass at each pixel from the MaxEnt model will not be normal.

To include upper and lower bounds to the biomass estimation, we also created biomass maps using the maximum and minimum values of each biomass class range instead of the median value. These maps are used to estimate the upper and lower bounds for national- and regional-level carbon stocks assessments.

Estimation of prediction uncertainty. The use of nonparametric models to develop AGB distributions is often subject to prediction errors. Unlike parametric models such as regression techniques where uncertainty can be readily quantified from the sensitivity of the measurement variables to predicting parameters, in nonparametric models, the prediction errors are potentially large and have complex spatial distributions.

We examined the MaxEnt model performance using two indicators: (*i*) the fraction of predicted area and extrinsic omission rate at a selected threshold and (*ii*) the area under the receiver operator curve (AUC) as a measure of model performance across all thresholds (12, 13). For all model runs, AUC values ranged between 0.86 and 0.98, suggesting that the predictions were significantly better than random (AUC = 0.5), with high statistical significance (one-tailed $P < 0.001$). This result was obtained by bootstrapping 25% of the training data (93,188 points) ~1,000 times, suggesting a robust performance of the MaxEnt algorithm to capture the variations in environmental variables to predict the probability distributions of biomass range classes.

To examine the presence of other potential errors such as the effect of the number of training pixels on MaxEnt performance, we developed several simulation runs by varying the number of training pixels. MaxEnt performance was optimal when a minimum of 100 training pixels were used for each biomass range run. This requirement was readily met when hundreds to several thousands of pixels were used in each biomass range.

Significance of remote sensing variables. The contribution of 14 remote sensing variables in modeling the distribution of AGB was evaluated by the jackknife test on all input variables and they were grouped and reported separately by geographic region in four AGB ranges (Fig. S3). We selected these biomass ranges on the basis of the sensitivity of the remote sensing data to detecting the spatial variations of AGB (13). The jackknife test was performed for all model runs and the significance of layers was reported in terms of percentage of explaining the total variability of each AGB range. We grouped 14 remote sensing variables in four types of observations or features that related to vegetation greenness and seasonality (5 NDVI metrics), leaf area index (3 LAI metrics), canopy roughness and water content and its seasonality (4 QSCAT metrics), and surface elevation and slope variations (2 SRTM metrics).

SRTM data contributed less than other variables in modeling AGB, with the highest contribution in Asia due to extensive topographic features in southeast islands of Indonesia and Papua New Guinea and in highlands of Nepal, Bhutan, and eastern China. Among other variables, the NDVI metrics had the largest contribution in low biomass density forests (<100 Mg ha^{-1}), the LAI metrics were important in midrange biomass density (100–200 and 200–300 Mg ha^{-1}), and the QSCAT metrics were important in all biomass ranges >100 Mg ha^{-1} with the largest contribution in modeling the high-density biomass forests. These contributions cannot be explained in terms of physical relationships between the remote sensing variables and the aboveground biomass density, yet they represent the relative significance of the remote sensing variables and their spatial and temporal characteristics to stratify the tropical landscapes in features that allow extrapolating the forest biomass density.

(iii) Uncertainty analysis. We calculated the overall uncertainty in the final benchmark map by quantifying the errors associated with the distribution of AGB and the estimation of BGB from AGB at the pixel and national or regional scales. We assumed no errors associated with converting the total biomass to carbon using a 50% conversion factor or with the original allometric equations that converted the ground forest structure to biomass. The total uncertainty of AGB at the pixel level is divided into four independent terms and all terms are reported in terms of percentage of relative uncertainty:

Measurement error ($\varepsilon_{measurement}$) is associated with the estimation of Lorey's height from GLAS Lidar data. For broadleaf forests, the RMSE has been estimated to be 3.3 m with the relative error of ~13.7% over the entire height range (20).

Allometric error ($\varepsilon_{allometric}$) refers to errors in estimating AGB from Lorey's height and was estimated from the relations developed from calibration plots. Regional allometric equations (Fig. 1) provided uncertainty in AGB estimation of 15.8% in Latin America, 21.7% in Africa, and 25.1% in Asia. The allometric errors are estimated for small areas representing the effective footprint of GLAS Lidar samples (0.25–0.5 ha).

Sampling error ($\varepsilon_{sampling}$) has two components: (*i*) the error associated with the representativeness of ground sampling plots and GLAS Lidar shots of the true distribution of the AGB in each region and (*ii*) the error associated with the AGB of a 1-km pixel due to the spatial variability of forest structure and biomass in a 1-km grid cell. The first component has been accounted for while quantifying the prediction error associated with the MaxEnt modeling of AGB. To quantify the second error, we require forest structure and biomass data over 1-km^2 (100 ha) plot sizes. In the absence of reliable data to quantify the sampling errors, we approximated the errors using published data for 50 ha of forest on Barro Colorado Island, Panama as a representative example of undisturbed tropical forest (21). Using a sampling unit of 0.25 ha (i.e., the area of one GLAS Lidar footprint), the AGB is approximately normally distributed around its mean (6). The variation of AGB within the 50-ha plot is high and has the mean SD of 128 Mg ha^{-1} and a 95% confidence interval of 20.1 Mg ha^{-1}. Using the sampling size equation for 95% confidence interval, Chave et al. (6) found the number of 0.25-ha or 0.5-ha plots required to estimate the biomass of a 50-ha plot with ±10% uncertainty varies between 16 (at 0.5 ha) and 26 (at 0.25 ha). By assuming the biomass of a 1-km pixel (100-ha) plot has the same variations as that of the 50-ha plot, and by using a minimum of five samples (GLAS Lidar shots), the uncertainty of AGB estimation with 95% confidence will increase and be bounded between 17.8% ($10 \times \sqrt{16/5}$) and 22.8% ($10 \times \sqrt{26/5}$). By examining the spatial variability of AGB in smaller plots (5–10 ha) available in Rondonia Brazil, Peru, Lope National Park in Gabon, and Sabah in Indonesia, we

were able to verify that variability did not exceed ±20%. A similar study by Chave et al. (22) in French Guiana using data from an 80-ha plot concluded that estimating the biomass of the entire plot with only a 1-ha plot will yield a typical error of ±20% due to spatial variability and sampling errors for capturing large trees.

Prediction error ($\varepsilon_{prediction}$) was calculated from prediction probabilities of the MaxEnt model. We used two approaches to quantify the prediction uncertainty. To estimate the average error or uncertainty, we used the 67,730 pixels with AGB values representing the mean AGB of a 1-km pixel. These estimates provided an average relative error in percentage of the mean AGB for pixels not used in training the spatial model (Fig. S4). To estimate the spatial uncertainty that resulted from the MaxEnt model, we used the predicted probability for each biomass range to calculate the root mean squared error,

$$\sigma_{\widehat{B}} = \sqrt{\frac{\sum_{i=1}^{N}(B_i - \widehat{B})^2 P_i}{\sum_{i=1}^{N} P_i}}, \qquad \textbf{[S5]}$$

with the relative uncertainty for each pixel given by: $\varepsilon_{prediction} = \sigma_{\widehat{B}} / \widehat{B} \times 100$. This relation is used for the entire AGB map, using the values of MaxEnt probabilities P_i for each biomass range class B_i and the predicted biomass value $\widehat{B}$. The prediction uncertainty includes both the sampling error associated with the representativeness of the training data of the actual spatial distribution of AGB and the model predictions.

Finally, we propagated the errors through the entire process by assuming all errors were independent and random and quantified the uncertainty in estimating AGB (ε_{AGB}) using

$$\varepsilon_{AGB} = \left(\varepsilon_{measurement}^2 + \varepsilon_{allometry}^2 + \varepsilon_{sampling}^2 + \varepsilon_{prediction}^2\right)^{1/2}, \quad \textbf{[S6]}$$

where all errors terms are the relative errors associated with the AGB at a pixel (23). The error propagation equation assumes that the errors are uncorrelated and on the average the covariant terms are neglected. To demonstrate the propagation of errors in modeling AGB of a 1-km pixel in Latin America, we use the measurement error of Lorey's height at 13.7% and calculate the relative error in AGB by multiplying the height relative error by 1.9701 using the equation given in Fig. 1B to arrive at 26.9%, allometric error of 15.7% to convert the Lorey's height to AGB, a maximum sampling error of 22.8%, and assuming a maximum prediction error of 21% at the pixel level, to arrive at the maximum relative error of AGB of 43.9%.

The uncertainty in total biomass carbon is calculated by combining the errors in AGB and BGB. The error in BGB is estimated from both the error in the prediction of BGB from AGB through the allometric Eq. S2 (23.2%) (9) and the error in AGB,

$$\varepsilon_{BGB} = \left[(23.2)^2 + (0.89\varepsilon_{AGB})^2\right]^{1/2}, \qquad \textbf{[S7]}$$

where ε_{BGB} is the relative uncertainty in BGB. The coefficient, 0.89 is the power of AGB in the allometric relationship used in Eq. S2 (9, 23). To estimate the uncertainty in total carbon at the pixel level, we use a similar equation to Eq. S6 to propagate the errors in estimating ε_{BC}, the relative uncertainty associated with the total biomass carbon (BC) defined by BC(Mg C ha^{-1}) = (AGB + BGB)/2.

Uncertainty at the national scale. Uncertainty at the national or regional scale is estimated by increasing the sample area and propagating the errors from pixel scale to the national or regional scale. We calculate the national- or regional-level SE (Mg C ha^{-1}) by summing the errors from all pixels using

$$\sigma_{national} = \sqrt{\sum_{i=1}^{N}(BC_i \varepsilon_{BC_i})^2}, \qquad \textbf{[S8]}$$

where N is the number of pixels within the national boundary, and BC_i and εBC_i are the total carbon and its relative uncertainty associated with pixel i, respectively. Although the SE is large at the national scale, the relative error declines rapidly as N increases according to

$$\varepsilon_{national} = \frac{\sigma_{national}}{\sum_{i=1}^{N} BC_i}. \qquad \textbf{[S9]}$$

The national-scale uncertainty analysis was also performed for variable size ($N \times N$) windows over the carbon map to examine the reduction of relative uncertainty as sampling size increases. We found the relative uncertainty stayed bounded below ±5% for $n = 10$ (10,000 ha) and below ±1% for $n = 100$ (1,000,000 ha) over the entire carbon map.

Uncertainty from forest spatial and temporal dynamics. The benchmark map represents the state of the carbon stock in forests for the year circa 2000. The coarse spatial resolution and the temporal changes in forest cover at the subpixel level due to deforestation dynamics may introduce uncertainty in carbon estimates. As the spatial unit of the map is 1 km, the spatial model underestimates the carbon density of the remaining forest for a pixel with subpixel forest cover.

In addition, satellite image data used to develop the spatial distribution of forest biomass are primarily from the period of 2000–2001 with >83% of pixels from the year 2000, ~16% from the year 2001, and a small fraction of pixels (<1%) extracted from subsequent years (2002–2003), which are largely over areas where forest cover has not changed for the period (25). However, the use of multitemporal imagery for modeling carbon distribution will introduce an uncertainty in carbon stocks of pixels that changed between 2000 and 2001. Both uncertainties from coarse spatial resolution and temporal imagery have almost no impact on evaluating the carbon stock at national or regional scales. However, they may introduce errors when estimating emissions from small-scale (<1 km) deforestation or degradation. These errors can be corrected by developing an area-correction factor for carbon density of pixels with subpixel forest cover change.

Comparison with published results. The comparison of the benchmark map with an earlier result over the Amazon Basin (ref. 14) was performed at three steps: (*i*) The earlier map was produced in biomass class range. The map was converted to continuous biomass numbers by choosing the median value of each biomass class at the pixel level and assigning zero values for bare and grass savanna classes. (*ii*) The difference between the two maps over the Amazon basin was calculated and values outside the uncertainty range of the benchmark map were colored for negative and positive differences. (*iii*) The maps were visually compared with the vegetation map of the Rio Negro basin of central Amazonia (25) where significant differences were observed over areas of swamp and white sand vegetation (Fig. S5). Lorey's height inferred from GLAS data over these forests is significantly lower than that over other terra firme forests in Amazonia because of their low stature and biomass density (26).

1. Zwally HJ, et al. (2002) ICESat's laser measurements of polar ice, atmosphere, ocean, and land. *J Geodyn* 34:405–445.
2. Harding DJ, Carabajal CC (2005) ICESat waveform measurements of within foot-print topographic relief and vegetation vertical structure. *Geophys Res Lett* 32:L21S10.
3. Lefsky MA, Keller M, Pang Y, de Camargo PB, Hunter HO (2007) Revised method for forest canopy height estimation from Geoscience laser Altimeter System waveforms. *J Appl Remote Sens* 1:013537.
4. Lefsky MA, et al. (2005) Estimates of forest canopy height and aboveground biomass using ICESat. *Geophys Res Lett* 32:L22S02.
5. Lefsky MA (2010) A global forest canopy height map from the Moderate Resolution Imaging Spectroradiometer and the Geoscience Laser Altimter System. *Geophys Res Lett* 37:L15401.
6. Myneni RB, et al. (2002) Global products of vegetation leaf area and fraction absorbed PAR from year one of MODIS data. *Remote Sens Environ* 83:214–231.
7. Chave J, et al. (2005) Tree allometry and improved estimation of carbon stocks and balance in tropical forests. *Oecologia* 145:87–99.
8. Feldpausch TR, et al. (2010) Height-diameter allometry for tropical forest trees. *Biogeosci Discuss* BGD-7:7727–7793.
9. Mokany K, Raison RJ, Prokushkin AS (2006) Critical analysis of root:shoot ratios in terrestrial biomes. *Glob Change Biol* 12:84–96.
10. Dungan JL, Peterson DL, Curran PJ (1994) Alterative approaches for mapping vegetation quantities using ground and image data. *Environmental Management and Analysis: Ecosystem to Global Scales*, eds Michener W, Brunt J, Stafford S (Taylor & Francis, London), pp 237–261.
11. Evans JS, Cushman SA (2009) Gradient modeling of conifer species using random forests. *Landscape Ecol* 24:673–683.
12. Philips S, Anderson RP, Schapire RE (2006) Maximum entropy modelling of species geographic distributions. *Ecol Modell* 190:231–259.
13. Phillips SJ, Dud'ık M, Schapire RE (2004) A maximum entropy approach to species distribution modeling. *Proceedings of the 21st International Conference on Machine Learning* (ACM Press, New York), pp 655–662.
14. Myneni RB, et al. (2007) Large seasonal swings in leaf area of Amazon rainforests. *Proc Natl Acad Sci USA* 104:4820–4823.
15. Huete AR, et al. (2002) Overview of the radiometric and biophysical performance of the MODIS vegetation indices. *Remote Sens Environ* 83:195–213.
16. Long DG, Drinkwater M, Holt B, Saatchi S, Bertoia C (2001) Global ice and land climate studies using scatterometer image data. *Eos Trans AGU* 82:503–504.
17. Rennó CD, et al. (2008) Hand, a new terrain descriptor using SRTM-DEM: Mapping terra-firme rainforest environments in Amazonia. *Remote Sens Environ* 112:3469–3481.
18. Rossetti DF, Toledo PM, Goes AM (2005) New geological framework for Western Amazonia (Brazil) and implications for biogeography and evolution. *Quat Res* 63:78–89.
19. Hansen MC, et al. (2002) Towards an operational MODIS continuous field of percent tree cover algorithm: examples using AVHRR and MODIS data. *Remote Sens Environ* 83:303–319.
20. Lefsky MA, et al. (2005) Estimates of forest canopy height and aboveground biomass using ICESat. *Geophys Res Lett* 32:L22S02.
21. Chave J, et al. (2003) Spatial and temporal variation in biomass of a tropical forest: Results from a large census plot in Panama. *J Ecol* 91:240–252.
22. Chave J, Bernard R, Dubois M-A (2001) Estimation of biomass in a new tropical forest of French Guiana: Spatial and temporal variability. *J Trop Ecol* 17:79–96.
23. Bevington P, Robinson DK (2003) *Data Reduction and Error Analysis for the Physical Sciences* (McGraw-Hill, New York).
24. Hansen MC, et al. (2008) Humid tropical forest clearing from 2000 to 2005 quantified by using multitemporal and multiresolution remotely sensed data. *Proc Natl Acad Sci USA* 105:9439–9444.
25. Veloso HP, Rangel Filho ALR, Lima JCA (1991) *Classifying the Vegetation of Brazil by Adapting a Universal System* [Instituto Brasilleiro de Geographia e Estatistica (IBGE), Rio de Janeiro, Brazil].
26. Pires JM, Prance GT (1985) The vegetation types of the Brazilian Amazon. *Key Environments: Amazonia*, eds Prance GT, Lovejoy TE (Pergamon, New York), pp 109–145.
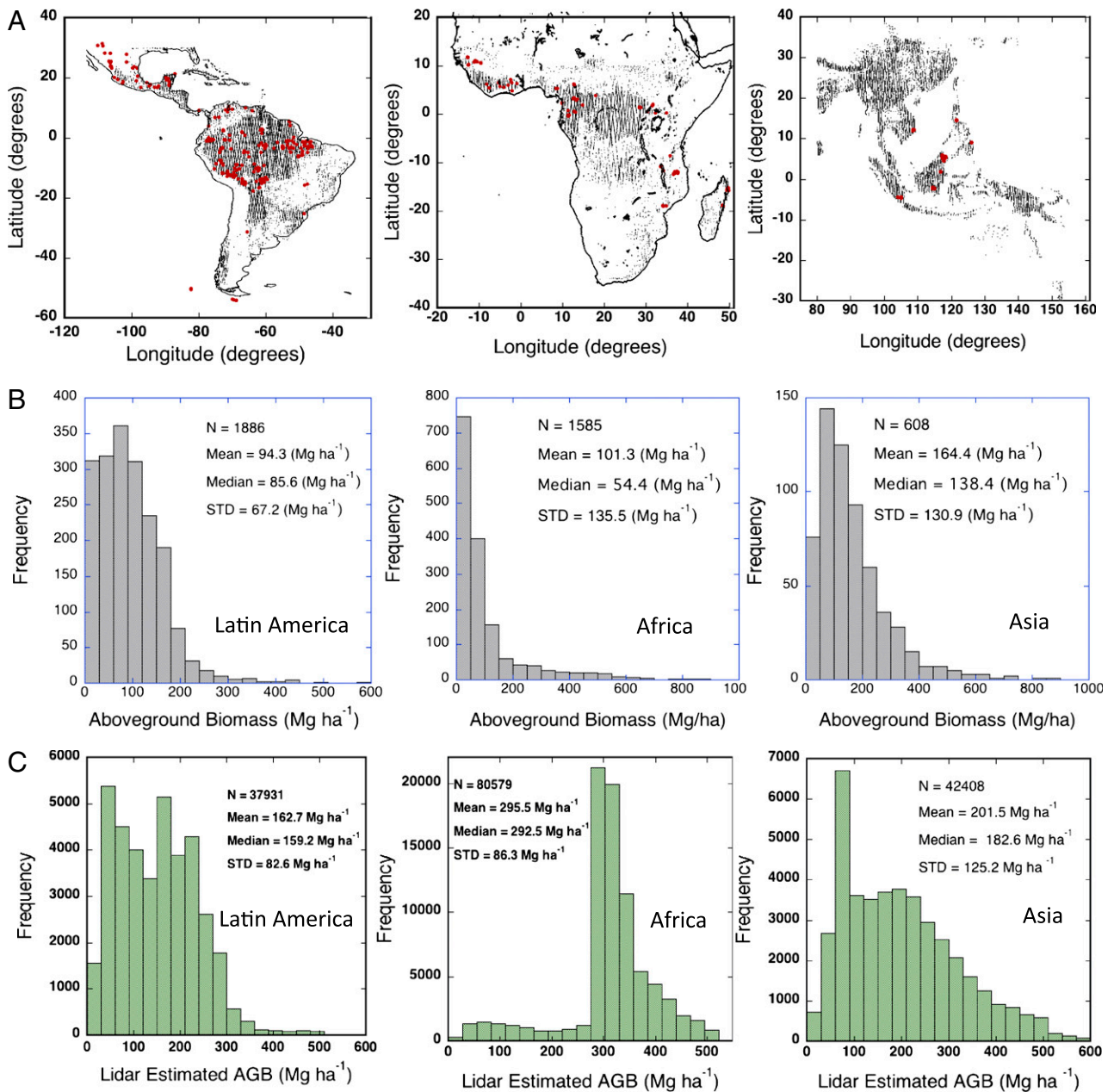
Fig. S1. Distribution of the location and magnitude of aboveground biomass values collected from in situ measurements and derived from GLAS Lidar data over tropical forests across three continents. (*A*) Geographical distribution of training and test data used in AGB spatial modeling with red dots representing the 1-km pixels associated with 4,079 in situ field plots and gray dots showing 160,918 pixels with AGB values derived from Lidar data across orbital tracks. (*B*) Distribution of AGB values from in situ data representing an uneven and unsystematic sampling of forest biomass across three continents. (*C*) Distribution of AGB values from GLAS Lidar data showing a widespread and representative sampling of AGB of forest types across three continents.
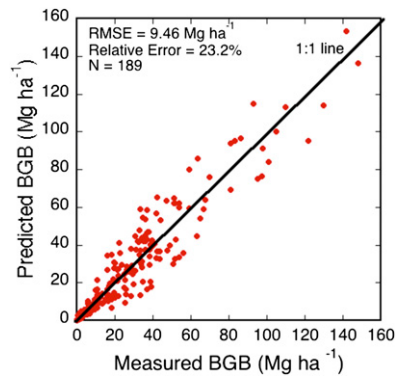
Fig. S2. Predicted versus measured BGB using an allometric equation and data from 189 field plots from Mokany et al. (9). The solid line shows the 1:1 relationship and the RMSE and the relative errors are calculated at 95% confidence interval from bootstrapping cross-validation. The data were obtained from Mokany et al. (9).
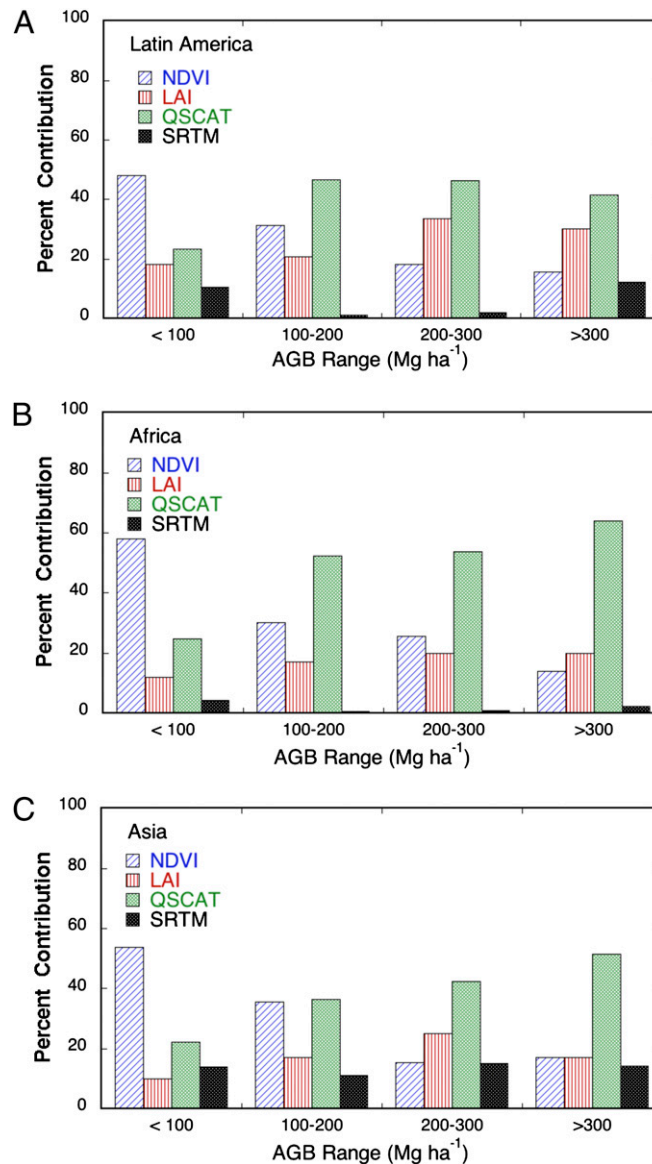

Fig. S3. Relative contribution of remote sensing variables in modeling the spatial variability of AGB. The contributions are calculated using jackknife analysis and shown for four categories of remote sensing observations and derived variables for (*A*) Latin America, (*B*) Africa, and (*C*) Asia. The remote sensing variables included in the analysis are five MODIS NDVI, three MODIS LAI, four QSCAT, and two SRTM derived metrics.
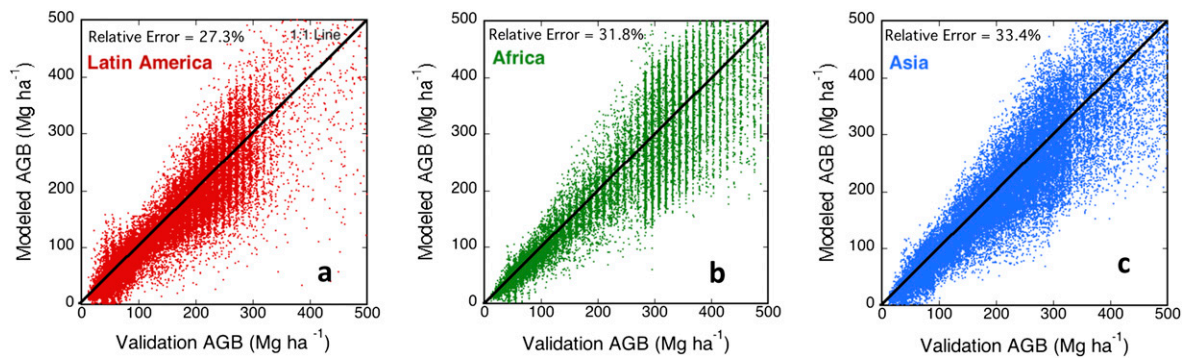
Fig. S4. (*A–C*) Assessment of the uncertainty of the spatial distribution of AGB from an independent validation data set of 67,730 points from a mixture of ground and GLAS Lidar estimated AGB. The uncertainty of the benchmark biomass map varied across AGB range and geographical regions, resulting an average uncertainty of ∼30% across three continents (27.3% in Latin America, 31.8% in Africa, and 33.4% in Asia).
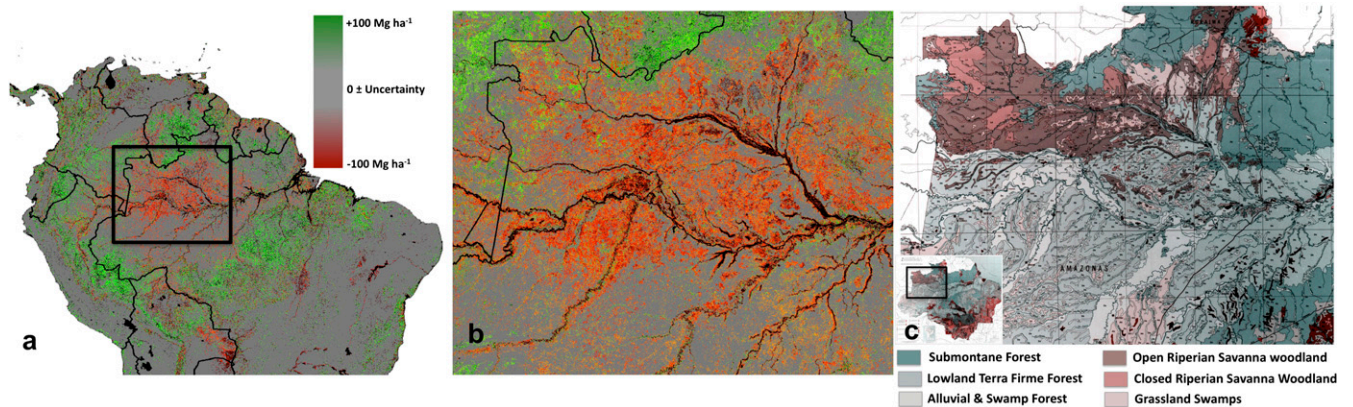
Fig. S5. Comparison of the benchmark map with the Amazon Basin biomass map (ref. 14: main text). (*A*) difference in AGB (Mg ha^{-1}) of benchmark and the earlier Amazon basin outside the uncertainty levels. (*B*) AGB difference in higher resolution selected over the Rio Negro Basin in central Amazonia. (*C*) Rio Negro vegetation types selected from the classification map of the Brazilian Amazon (25).

Table S1. List of ground biomass plot data used in this study with their general location, number of plots, plot size, vegetation types, and references or plot ownerships

Table S1 (DOC)

Table S2. List of calibration plots and their general locations used in developing height biomass allometry

Table S2 (DOCX)

The national-level estimates for each tree cover threshold are provided for low, mean, and high values by integrating the potential systematic errors associated with pixel (1-km)-level biomass carbon estimates. Estimates for 75 developing countries in tropical regions across three continents are shown. For Caribbean islands, we report total biomass carbon estimates.

Table S3. National level forest area and biomass carbon estimates at three tree cover thresholds of (*a*) 10%, (*b*) 25%, and (*c*) 30%

Table S3 (DOC)

The national level estimates for each tree cover threshold are provided for low, mean, and high values by integrating the potential systematic errors associated with pixel (1-km) level biomass carbon estimates. The table includes estimates for 75 developing countries in tropical regions across three continents. For Caribbean islands, we report total biomass carbon estimates.